SCEC PROJECT TECHNICAL REPORT 25225: Measuring differential uplift across multiple fault strands in the San Gorgonio Pass region using thermoluminescence thermochronology

PI: Nathan Brown, University of Texas at Arlington

1 Summary

The San Gorgonio Pass (SGP) is a structurally complex and incompletely understood region of the southern San Andreas fault zone. There is ongoing debate regarding how slip is partitioned among various strands in this region and which faults may produce large earthquakes (Kendrick et al., 2015, 2022; Heermance and Yule, 2017; Fosdick and Blisniuk, 2018; Blisniuk et al., 2021; Yule et al., 2021). One reason for this uncertainty is the lack of datable material due steep, mountainous topography surrounding the traces of these faults. Few sedimentary deposits are preserved in this landscape and therefore relatively few offset geomorphic units or paleoseismic trench sites have been investigated to inform recent slip activity for these fault strands through the SGP on Late Quaternary timescales (e.g., Fig. 1 of Heermance and Yule, 2017).

Rather than dating tectonically offset sedimentary deposits to constrain recent deformation, an alternative approach is to measure bedrock erosion rates throughout the SGP to identify systematic differences in erosion rates across fault strands. Both low-temperature apatite (U-Th)/He (AHe) thermochronology of bedrock outcrops (Spotila et al., 1998, 2001) and catchment-averaged denudation rates from cosmogenic ^{10}Be in stream sediments (Binnie et al., 2007, 2008, 2010; Argueta et al., 2024) have shown that the primary control on bedrock erosion within the San Bernardino Mountains on timescales of 1-100 ka is the distribution of crustal uplift, with the broad regional trend of increasing erosion rates towards the south, approaching the San Bernardino strand of the San Andreas fault.

This project adds ten new thermoluminescence (TL) thermochronology samples from the southeastern end of the Yucaipa Ridge block, near the Galena Peak, Mission Creek and San Bernardino strands (circle symbols in Fig. 1 with exact locations in Table 1). Assuming a geothermal gradient of 30°C/km (Lachenbruch et al., 1985), we infer average erosion rates on 10 - 100 ka timescales, in 10 ka bins (Tables 2 and 3). Considering the maximum erosion rates for each sample throughout the entire 10 - 100 ka interval, samples adjacent to all nearby fault strands (Mill Creek, Mission Creek San Bernardino) have experienced elevated erosion rates compared to samples farther from fault traces (Fig. 1c). Fault strands exhibit elevated erosion at different time intervals, however. In the oldest resolved time period, 90 - 100 ka, the eastern end of the Mill Creek strand exhibits elevated erosion (Fig. 1b), whereas in the youngest period, 10 - 20 ka, the eastern-most cluster of samples near the Mill Creek strand experienced a relatively low erosion rate. This stands in contrast to samples from the western side of this fault zone, which have significantly elevated erosion, even recently. Some symbols in Fig. 1b are open, meaning that no cooling ages were determined within this time interval. Thus no erosion rates are inferred for this time interval. This requires that significant erosion (more precisely, significant cooling) has affected these samples since 100 ka, but leaves unconstrained the erosion rate from 90 - 100 ka. *If bedrock erosion rates in this region are driven by tectonics*, as has been previously suggested (Binnie et al., 2010), two plausible conclusions from these data are that:

1. tectonic activity along the eastern Mill Creek has lessened during the 100 ka interval, whereas activity on the western portion of this strand remains high until at least 10 ka; and

2. tectonic activity along the San Bernardino strand (east of the junction with Mission Creek strand), the Mission Creek strand, and the Galena Peak strand remains high until 10 ka.

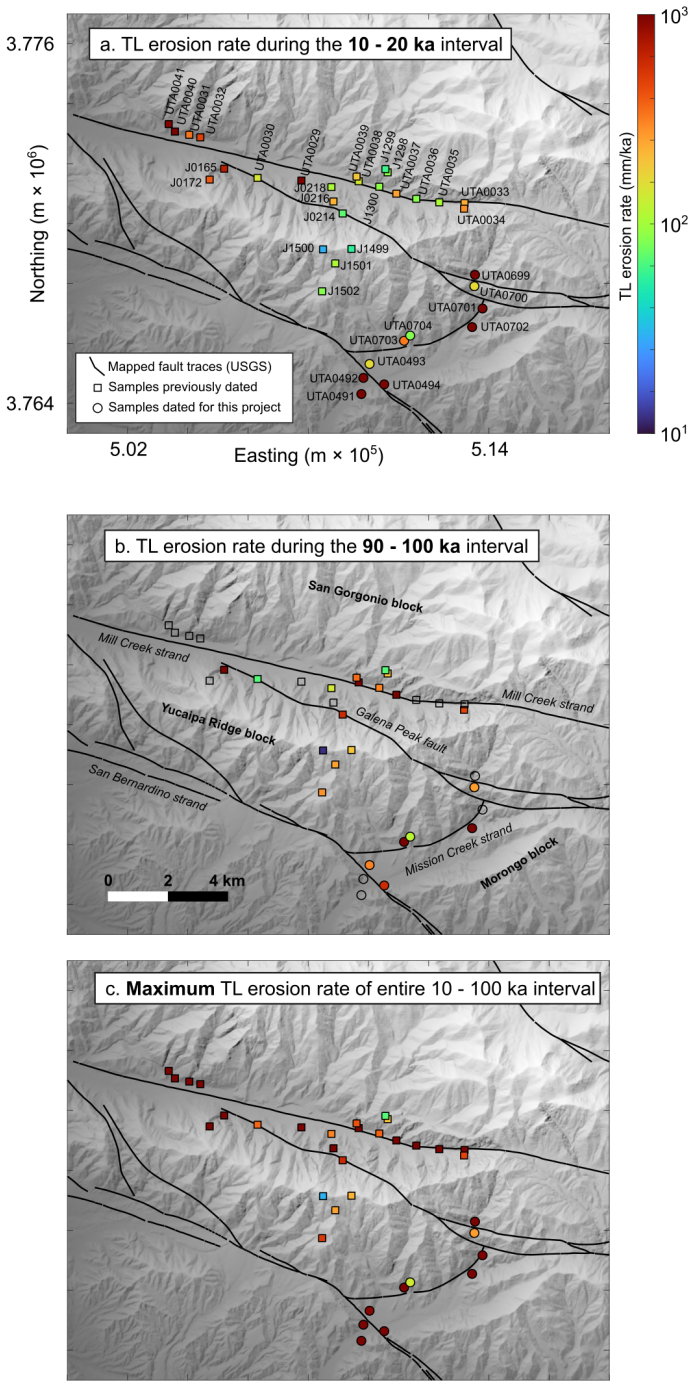

Figure 1: Thermoluminescence (TL) sample locations collected previously (squares) and for this study (circles) are colored by their apparent erosion rates. These are shown for: (a) the most recent resolved time period of 10-20 ka, (b) the oldest resolved time period of 90-100 ka, and (c) the maximum erosion rate within the entire 10-100 ka interval. Sample names are shown in (a) and major structures are shown in (b).

2 Sample and measurement details

Results are shown for several suites of samples (Table 1), beginning with those collected by Ed Rhodes at UCLA around 2011 (samples in the range of J0165 - J0218), by myself and Seulgi Moon and analyzed at UCLA (J1298 - J1300) and UTA (UTA0029 - UTA0041), by Mike Oskin at UC Davis then analyzed by myself at UCLA (J1499 - J1502) and then finally, those collected for this project by myself and my PhD student Ayush Joshi and analyzed at UTA (UTA0491 - UTA0494; UTA0699 - UTA0704). All of these samples were collected from in place bedrock outcrops (not 'float') using a hammer and chisel. Therefore all thermochronology results are interpreted to represent an *in situ* cooling history.

Sample preparation and luminescence measurements were performed at the UTA luminescence lab. Under dim amber light conditions, the light-exposed outer surfaces of the rocks were sawn off and then the inner portion was disaggregated by mortar and pestle to isolate grains that were affected not by sunlight exposure but by geothermal heat exposure. These grains were then wet sieved, and separated by heavy liquid to isolate grains with density < 2.565 g/cm^3. The elemental compositions of samples were measured by inductively coupled plasma mass spectrometry and atomic emission spectroscopy, performed at SGS Canada. Geologic dose rates were calculated with the DRAC online calculator (Durcan et al., 2015).

The luminescence measurements performed in this study are described in detail in Brown and Rhodes (2022) and summarized here. To characterize the dose-response characteristics of each sample, 18 aliquots were measured for each of the bedrock samples. Additive doses were: 0 ($n = 9$; natural dose only), 50 ($n = 1$), 100 ($n = 1$), 500 ($n = 1$), 1000 ($n = 3$), and 5000 Gy ($n = 3$). Discs were heated from 0 to 500 °C at a rate of 0.5 °C/s, with TL intensity recorded at 1 °C increments, i.e., each channel integrates counts over 2 s. To quantify room-temperature signal fading, we prepared 10 natural aliquots per sample. These aliquots were first preheated to 100 °C for 10 s at a rate of 10 °C/s and then heated to 310 °C at a rate of 0.5 °C/s. Following these initial heatings, aliquots were given a beta dose of 50 Gy, preheated to 100 °C for 10 s at a rate of 10 °C/s and then held at room temperature for a set time (Auclair et al., 2003). Per sample, two aliquots each were stored for times of approximately 3 ks, 10 ks, 2 d, 1 wk and 3 wk. Following these storage times, aliquots were measured to quantify signal fading.

After determining sample-specific luminescence kinetic parameters, we calculated fading-corrected cooling ages for each TL measurement temperature bin as well as the effective closure temperature for each bin, using a forward numerical model. Combining these with the estimated local geothermal gradient of 30 °C/km (Lachenbruch et al., 1985), we estimate exhumation rates for the range of apparent closure ages within the TL temperature range of 220 - 300 °C. These results are then summarized in 10 ka bins from 10 - 100 ka. Some samples yield cooling ages >100 ka, but many do not. Below 10 ka, an yet-unexplained experimental artefact arises. So this was taken as a useful time range for comparison among samples.

3 Results

All apparent erosion rates are reported in Tables 2 and 3. Erosion rates are also shown by color (logarithmic scale) according to sample location in Fig. 1.

Table 1: Sample locations.

Sample	Lat (DD)	Lon (DD)
J0165	34.08726	-116.94354
J0172	34.08398	-116.94877
J0214	34.07375	-116.90090
J0216	34.07737	-116.90422
J0218	34.08170	-116.90495
J1298	34.08610	-116.88470
J1299	34.08710	-116.88550
J1300	34.08180	-116.88770
J1499	34.06309	-116.89775
J1500	34.06296	-116.90797
J1501	34.05873	-116.90358
J1502	34.05034	-116.90832
UTA0029	34.08367	-116.91575
UTA0030	34.08448	-116.93153
UTA0031	34.09747	-116.95610
UTA0032	34.09669	-116.95213
UTA0033	34.07682	-116.85703
UTA0034	34.07515	-116.85720
UTA0035	34.07707	-116.86612
UTA0036	34.07815	-116.87440
UTA0037	34.07970	-116.88157
UTA0038	34.08343	-116.89513
UTA0039	34.08485	-116.89588
UTA0040	34.09843	-116.96127
UTA0041	34.10068	-116.96352
UTA0491	34.01941	-116.89423
UTA0492	34.02426	-116.89349
UTA0493	34.02846	-116.89405
UTA0494	34.02231	-116.88601
UTA0699	34.05523	-116.85330
UTA0700	34.05182	-116.85353
UTA0701	34.04509	-116.85061
UTA0702	34.03952	-116.85436
UTA0703	34.03542	-116.87883
UTA0704	34.03699	-116.87664

Table 2: Unpublished TL erosion rates from previous work.

	TL erosion rate (mm/ka) from t to $t+10$ ka (95% CI) where t :								
Sample	10	20	30	40	50	60	70	80	90
J0165	683^{+315}_{-180}	991^{+416}_{-224}	769^{+102}_{-179}	476^{+72}_{-62}	641^{+114}_{-146}	1219^{+298}_{-250}	691^{+177}_{-324}	1313^{+479}_{-467}	1558
J0172	400^{+31}_{-27}	850^{+132}_{-112}	2515^{+442}_{-377}	4726^{+997}_{-681}	2639^{+1150}_{-689}	-	-	-	-
J0214	70^{+5}_{-4}	66^{+8}_{-4}	63^{+8}_{-7}	103^{+25}_{-27}	118^{+54}_{-34}	313^{+169}_{-138}	255^{+33}_{-50}	378^{+171}_{-227}	601^{+276}_{-249}
J0216	225^{+102}_{-59}	373^{+92}_{-97}	883^{+634}_{-425}	610^{+221}_{-197}	291^{+101}_{-101}	505^{+163}_{-172}	1573^{+1495}_{-932}	-	-
J0218	107^{+5}_{-5}	130^{+5}_{-6}	180^{+10}_{-17}	308^{+103}_{-80}	247^{+24}_{-25}	217^{+10}_{-11}	220^{+15}_{-17}	169^{+10}_{-10}	141^{+19}_{-19}
J1298	89^{+3}_{-4}	82^{+2}_{-2}	81^{+2}_{-1}	88^{+3}_{-4}	96^{+2}_{-4}	116^{+8}_{-14}	127^{+4}_{-2}	172^{+64}_{-32}	199^{+39}_{-30}
J1299	61^{+2}_{-3}	54^{+1}_{-2}	53	51^{+1}_{-1}	54^{+2}_{-1}	55^{+2}_{-2}	56^{+2}_{-2}	67^{+3}_{-3}	68^{+2}_{-3}
J1300	89^{+2}_{-2}	90^{+1}_{-2}	98^{+3}_{-3}	116^{+4}_{-5}	149^{+13}_{-9}	227^{+16}_{-11}	382^{+47}_{-63}	325^{+10}_{-11}	309^{+23}_{-40}
J1499	55^{+1}_{-1}	54^{+0}_{-1}	58^{+2}_{-1}	69^{+5}_{-8}	81^{+5}_{-6}	118^{+17}_{-13}	192^{+34}_{-30}	228^{+35}_{-37}	195^{+23}_{-27}
J1500	30^{+2}_{-2}	23^{+1}_{-1}	20^{+1}_{-0}	17^{+1}_{-1}	16	15	14	13	12
J1501	108^{+3}_{-2}	102^{+2}_{-3}	104^{+2}_{-1}	115^{+7}_{-8}	136^{+7}_{-9}	155^{+13}_{-8}	193^{+10}_{-12}	222^{+22}_{-18}	252^{+22}_{-18}
J1502	85^{+2}_{-1}	81^{+1}_{-1}	93^{+8}_{-4}	117^{+6}_{-3}	192^{+30}_{-20}	499^{+96}_{-106}	521^{+61}_{-47}	468^{+91}_{-85}	283^{+25}_{-25}
UTA0029	1744^{+1049}_{-629}	1507^{+1000}_{-580}	1239^{+917}_{-398}	-	-	-	-	-	-
UTA0030	144^{+93}_{-72}	366^{+246}_{-149}	177^{+169}_{-105}	332^{+188}_{-145}	157^{+130}_{-91}	109^{+90}_{-76}	86	79^{+53}_{-53}	68
UTA0031	335^{+12}_{-14}	395^{+25}_{-14}	509^{+34}_{-40}	842^{+102}_{-103}	2237^{+501}_{-445}	4741^{+3626}_{-2154}	2787^{+1035}_{-1727}	-	-
UTA0032	487^{+171}_{-151}	1331^{+933}_{-563}	1211^{+895}_{-571}	976^{+605}_{-384}	659^{+271}_{-271}	-	-	-	-
UTA0033	234^{+57}_{-38}	2278^{+996}_{-659}	1794^{+1165}_{-756}	-	-	-	-	-	-
UTA0034	286^{+119}_{-136}	31^{+6}_{-5}	44^{+7}_{-13}	32^{+5}_{-7}	48^{+7}_{-7}	49^{+22}_{-42}	117^{+38}_{-50}	282^{+242}_{-272}	464^{+330}_{-332}
UTA0035	107^{+11}_{-10}	1036^{+1521}_{-747}	759^{+832}_{-258}	$87959^{+143898}_{-57967}$	-	-	-	-	-
UTA0036	86^{+3}_{-5}	103^{+9}_{-7}	186^{+32}_{-37}	248^{+28}_{-32}	497^{+217}_{-161}	4691^{+5555}_{-2885}	2170^{+540}_{-496}	-	-
UTA0037	256^{+11}_{-8}	313^{+16}_{-16}	430^{+47}_{-31}	447^{+84}_{-62}	718^{+179}_{-138}	640^{+122}_{-105}	898^{+130}_{-131}	1892^{+892}_{-951}	1348^{+549}_{-385}
UTA0038	143^{+7}_{-7}	172^{+19}_{-21}	223^{+24}_{-19}	378^{+61}_{-45}	353^{+54}_{-60}	546^{+131}_{-117}	362^{+391}_{-222}	6236^{+3616}_{-3726}	1500^{+532}_{-495}
UTA0039	197^{+6}_{-5}	203^{+6}_{-7}	270^{+36}_{-33}	276^{+22}_{-17}	349^{+57}_{-45}	402^{+73}_{-80}	381^{+28}_{-23}	414^{+53}_{-57}	353^{+17}_{-27}
UTA0040	2337^{+1520}_{-895}	8239^{+7367}_{-4227}	1293^{+1008}_{-465}	2367^{+2456}_{-888}	3992^{+4517}_{-2844}	-	-	-	-
UTA0041	956^{+63}_{-55}	2119^{+1104}_{-770}	5761^{+5438}_{-2973}	-	-	-	-	-	-

Table 3: TL erosion rates from this project.

	TL erosion rate (mm/ka) from t to $t+10$ ka (95% CI) where t :								
Sample	10	20	30	40	50	60	70	80	90
UTA0491	1552^{+288}_{-239}	938^{+194}_{-157}	4263^{+3076}_{-2406}	1499^{+562}_{-678}	591^{+449}_{-301}	333^{+322}_{-199}	1189^{+954}_{-862}	-	-
UTA0492	13554^{+12218}_{-8513}	7369^{+4086}_{-4091}	13461^{+8018}_{-8142}	583^{+214}_{-393}	358^{+297}_{-200}	999^{+620}_{-757}	2132	-	-
UTA0493	161^{+9}_{-11}	268^{+41}_{-35}	435^{+109}_{-144}	548^{+98}_{-100}	944^{+408}_{-320}	489^{+331}_{-272}	804^{+141}_{-239}	625^{+263}_{-423}	310^{+214}_{-169}
UTA0494	2103^{+812}_{-542}	1886^{+419}_{-312}	1375^{+633}_{-633}	2428^{+604}_{-308}	1821^{+333}_{-169}	3072^{+1795}_{-1878}	-	901^{+726}_{-469}	591
UTA0699	1658^{+1103}_{-656}	939^{+466}_{-463}	12495^{+9110}_{-6211}	904^{+1280}_{-507}	184^{+127}_{-77}	-	-	-	-
UTA0700	1658^{+1120}_{-632}	939^{+424}_{-482}	12495^{+8982}_{-6046}	904^{+1296}_{-511}	184^{+127}_{-77}	-	-	-	-
UTA0701	1008^{+460}_{-393}	2247^{+1359}_{-1141}	859^{+401}_{-296}	559^{+429}_{-251}	493^{+688}_{-347}	3457^{+1826}_{-1473}	1344^{+2}_{-2}	-	-
UTA0702	3756^{+2117}_{-1579}	1228^{+433}_{-396}	7307^{+4689}_{-4699}	1370^{+677}_{-779}	681^{+695}_{-540}	821^{+507}_{-507}	271^{+311}_{-159}	126^{+50}_{-50}	1354^{+101}_{-101}
UTA0703	326^{+56}_{-52}	284^{+76}_{-40}	282^{+76}_{-44}	371^{+57}_{-59}	304^{+84}_{-136}	2384^{+1240}_{-1342}	531^{+49}_{-29}	457^{+90}_{-139}	4218^{+1307}_{-3900}
UTA0704	84^{+5}_{-6}	75^{+5}_{-6}	85^{+9}_{-10}	80^{+5}_{-5}	104^{+11}_{-20}	85^{+2}_{-4}	137^{+5}_{-8}	102^{+8}_{-10}	116^{+17}_{-9}

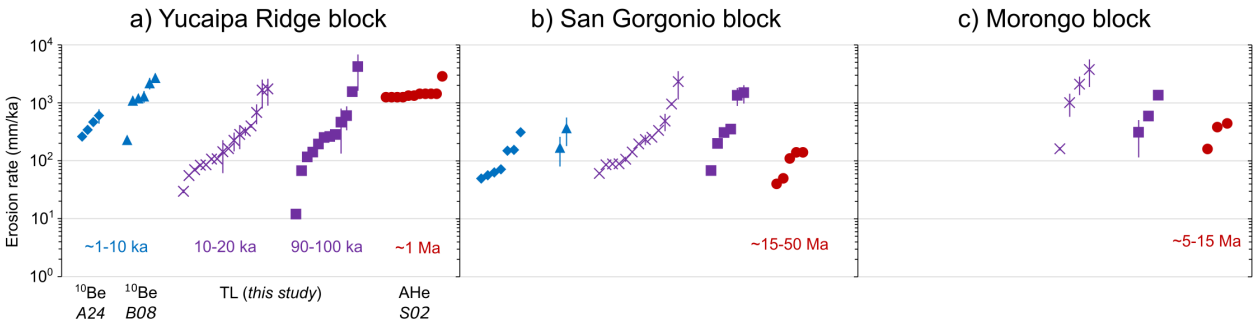

Figure 2: Erosion rates are plotted for samples collected from the (a) Yucaipa Ridge, (b) San Gorgonio, and (c) Morongo tectonic blocks. Basin-averaged cosmogenic ^{10}Be samples are shown from Argueta et al. (2024) (A24) and Binnie et al. (2008) (B08). Apatite (U-Th)/He samples are shown from Spotila et al. (2002) (S02). TL results are shown for the 10-20 and 90-100 ka intervals. The relevant averaging timescales are shown below each dataset.

Comparison between TL, apatite (U-Th)/He, and Be-10 erosion rate estimates

For the Yucaipa Ridge, San Gorgonio, and Morongo tectonic blocks, the erosion rates inferred from TL measurements on 10 - 100 ka timescales are broadly comparable to previously published erosion rates observed on millennial timescales from basin-averaged cosmogenic ^{10}Be (Binnie et al., 2010; Argueta et al., 2024) and also to million-year timescales from apatite helium thermochronometry (Spotila et al., 2001), as shown in Fig. 2. This absolute rate agreement among different geochronometers which are sensitive to different length and timescales is both expected and encouraging. Specifically, basin-averaged cosmogenic ^{10}Be rates integrate erosion over approximately 60 cm, with an averaging time inversely proportional to the erosion rate (Lal, 1991). In other words, the apparent erosion rate applies only for the time period required to erode away the mean attenuation length. For apatite helium (U-Th) thermochronology, the length scale is the effective closure depth (Dodson, 1973), which is on the order of a km or two, depending on the local geothermal gradient (Wolf et al., 1998). The time required to exhume samples from this depth (the so-called 'cooling age') ranges from about 1 - 50 Ma, with the Yucaipa Ridge block representing the young end of the spectrum and the San Gorgonio block at the old end. TL thermochronology integrates exhumation over 10 - 100 ka and over a depth range of hundreds of meters. Finally, these results represent different spatial averaging effects. Cosmogenic ^{10}Be from stream sediments (all samples discussed here) represent sediment contribution from the entire upstream area, including all landscape denudation processes that mobilize sediments, such as mass wasting events (Yanites et al., 2009). Apatite helium thermochronometry is an in situ, outcrop-based measurement, like luminescence. The difference in closure depths between TL and AHe techniques, however, means that TL results are sensitive to shorter-wavelenth topographic changes (Reiners and Shuster, 2009).

With these specifics in mind, we consider the instances where these different geo- and thermochronometers diverge. For the Yucaipa Ridge block (Fig. 2a), AHe results are more uniform than the other techniques, at a high mean value of just over 1000 mm/ka. These AHe values are tightly spatially clustered on the western end of the block, descending one spur of the mountain (ex. Fig. 2 of Spotila et al., 2002). Our TL erosion rates are generally higher on the western end of this block, compared to the east. But I hypothesize that the greater variability in apparent erosion rates within this block is likely meaningful. The lowest erosion rates are found on the ridgetop samples, with the lowest of all (J1500) being located on a relict surface which appears erosionally disconnected from the landscape, similar to samples J1298 and J1299 on the San Gorgonio block. Argueta

et al. (2024) recently argued that topographic disequilibrium is an important feature of landscapes throughout the San Bernardino Mountains, with some reaches of the landscape responding sensitively to erosional downcutting by streams or mass wasting, and other isolated patches experiencing anomalously low erosion rates. The varied erosional response of these tectonic blocks indicates that while tectonics do seem to ultimately set the pace of erosion in this region (Binnie et al., 2010), not all locations on a block will erode uniformly. An important implication is that blocks should be widely sampled to capture the full range of erosion rates.

Implications for seismic hazard

When this study was proposed, I hoped we might observe systematic differences of erosion rates across fault strands, in order to infer dip-slip during certain time intervals. With our current dataset, what we observe instead is significant *within-block* erosional variability, more so than the *between-block* variability that I hoped for. I think this is consistent with the growing dataset of basin-averaged ^{10}Be results from this region (Argueta et al., 2024).

Two spatial patterns emerge from these TL erosion rates. First, erosion rates in the 10-20 ka interval are much higher in the western Mill Creek region compared to the eastern end (Fig. 1a). This is not the case in the 90-100 ka interval, where samples along the eastern Mill Creek strand have high erosion rates. Although few samples in the west yield cooling ages as old as this, those nearby samples (J0172, UTA0031, UTA0032, UTA0040, UTA0041) exhibit high erosion rates over all resolved time intervals (up to 60, 80, 60, 60, and 40 ka, respectively; see Table 2).

Second, erosion rates adjacent to the Galena Peak, Mission Creek, and San Bernardino strands exhibit among the highest observed erosion rates in the 10-20 ka time interval (Fig. 1a). This is also true for the Mill Creek strand, but only west of the junction with the Galena Peak fault. East of this junction, erosion rates are relatively low. Both of these observations are consistent with the hypothesis that the eastern Mill Creek strand deactivated in the Late Pleistocene (Kendrick et al., 2022).

4 Dissemination

A preliminary version of these results were presented at the 2025 SCEC Annual Meeting (Joshi et al., 2025b) and the GSA Annual Meeting (Joshi et al., 2025a). The results will comprise a portion of UTA Ph.D. student Ayush Joshi's dissertation and we are currently preparing a manuscript for submission.

References

Argueta, M.O., Moon, S., Blisniuk, K., Brown, N.D., Corbett, L.B., Bierman, P.R., Zimmerman, S.R.H., 2024. Examining the influence of disequilibrium landscape on millennial-scale erosion rates in the san bernardino mountains, california, usa. GSA Bulletin .

Auclair, M., Lamothe, M., Huot, S., 2003. Measurement of anomalous fading for feldspar IRSL using SAR. Radiat. Meas. 37, 487–492.

Binnie, S.A., Phillips, W.M., Summerfield, M.A., Fifield, L.K., 2007. Tectonic uplift, threshold hillslopes, and denudation rates in a developing mountain range. Geology 35, 743–746.

Binnie, S.A., Phillips, W.M., Summerfield, M.A., Fifield, L.K., Spotila, J.A., 2008. Patterns of denudation through time in the San Bernardino Mountains, California: Implications for early-stage orogenesis. Earth Planet. Sci. Lett. 276, 62–72.

Binnie, S.A., Phillips, W.M., Summerfield, M.A., Fifield, L.K., Spotila, J.A., 2010. Tectonic and climatic controls of denudation rates in active orogens: The San Bernardino Mountains, California. Geomorphology 118, 249–261.

Blisniuk, K., Scharer, K., Sharp, W.D., Burgmann, R., Amos, C., Rymer, M., 2021. A revised position for the primary strand of the Pleistocene-Holocene San Andreas fault in southern California. Science Advances 7.

Brown, N.D., Rhodes, E.J., 2022. Developing an internally consistent methodology for K-feldspar MAAD TL thermochronology. Radiation Measurements 153, 106751.

Dodson, M., 1973. Closure temperature in cooling geochronological and petrological systems. Contrib. Mineral. Petrol. 40, 259–279.

Durcan, J.A., King, G.E., Duller, G.A.T., 2015. DRAC: Dose Rate and Age Calculator for trapped charge dating. Quat. Geochronol. 28, 54–61.

Fosdick, J.C., Blisniuk, K., 2018. Sedimentary signals of recent faulting along an old strand of the San Andreas Fault, USA. Scientific Reports 8, 12132.

Heermance, R.V., Yule, D., 2017. Holocene slip rates along the san andreas fault system in the san gorgonio pass and implications for large earthquakes in southern california. Geophysical Research Letters 44, 5391–5400.

Joshi, A., Brown, N.D., Moon, S., Argueta, M.O., 2025a. Investigating landscape response to tectonic reorganisation in the San Gorgonio Pass region using thermoluminescence (TL) thermochronology, in: Oral presentation at GSA Annual Meeting.

Joshi, A., Brown, N.D., Moon, S., Argueta, M.O., 2025b. Late Quaternary Erosion Rates in the San Gorgonio Pass: Insights From Thermoluminescence Thermochronology, in: Poster presentation at SCEC Annual Meeting.

Kendrick, K.J., j. C. Matti, Mahan, S.A., 2015. Late Quaternary slip history of the Mill Creek strand of the San Andreas fault in San Gorgonio Pass, southern California: The role of a subsidiary left-lateral fault in strand switching. Geol. Soc. Am. Bull. 127, 825–849.

Kendrick, K.J., Matti, J.C., Barth, N.C., 2022. Geologic and geomorphic evidence for multi-phase history of strands of the san andreas fault through the san gorgonio pass structural knot, southern california. Geosphere , 1–34.

Lachenbruch, A.H., Sass, J.H., Galanis, S.P., 1985. Heat flow in southernmost California and the origin of the Salton Trough. J. Geophys. Res. 90, 6709–6736.

Lal, D., 1991. Cosmogenic ray labeling of erosion surfaces: in situ nuclide production rates and erosion models. Earth Planet. Sci. Lett. 104, 424–439.

Reiners, P.W., Shuster, D.L., 2009. Thermochronology and landscape evolution. Physics Today , 31–36.

Spotila, J., Farley, K., Sieh, K., 1998. Uplift and erosion of the San Bernardino Mountains associated with transpression along the San Andreas fault, California, as constrained by radiogenic helium thermochronometry. Tectonics 17, 360–378.

Spotila, J., Farley, K., Yule, J., Reiners, P., 2001. Near-field transpressive deformation along the San Andreas fault zone in southern California, based on exhumation constrained by (U-Th)/He dating. J. Geophys. Res. 106, 30909–30922.

Spotila, J.A., House, M.A., Blythe, A.E., Niemi, N.A., Bank, G.C., 2002. Contributions to Crustal Evolution of the Southwestern United States. GSA. chapter Controls on the erosion and geomorphic evolution of the San Bernardino and San Gabriel Mountains, southern California. pp. 205–230.

Wolf, R., Farley, K., Kass, D., 1998. Modeling of the temperature sensitivity of the apatite (U–Th)/He thermochronometer. Chem. Geol. 148, 105–114.

Yanites, B.J., Tucker, G.E., Anderson, R.S., 2009. Numerical and analytical models of cosmogenic radionuclide dynamics in landslide-dominated drainage basins. J. Geophys. Res. 114, 1–20.

Yule, D., Matti, J.C., Kendrick, K.J., Heermance, R.V., 2021. Where's the slip? No slip in at least 40,000 years on northern-route strands of the San Andreas fault northwest of the Indio Hills, southern California, in: Poster presentation at SCEC Annual Meeting.